HHS Public Access

Author manuscript

Nat Methods. Author manuscript; available in PMC 2020 May 25.

Published in final edited form as:

Nat Methods. 2020 February ; 17(2): 201–208. doi:10.1038/s41592-019-0651-0.

In situ structure determination at nanometer resolution using TYGRESS

Kangkang Song[1,3,5], **Zhiguo Shang**[1,3], **Xiaofeng Fu**[1,4,6], **Xiaochu Lou**[1,4], **Nikolaus Grigorieff**[2], **Daniela Nicastro**[1,*]

[1]Departments of Cell Biology and Biophysics, University of Texas Southwestern Medical Center, Dallas, TX 75390, USA.

[2]Janelia Farm Research Campus, Howard Hughes Medical Institute, 19700 Helix Drive, Ashburn, VA 20147, USA.

[3]These authors contributed equally to this work.

[4]These authors contributed equally to this work.

[5]Current address: Cryo-EM Core Facility, University of Massachusetts Medical School, Worcester, MA 01655.

[6]Current address: Biological Science Imaging Resource, Florida State University, Tallahassee, FL 32306.

Abstract

The resolution of subtomogram averages calculated from cryo-electron tomograms (cryo-ET) of crowded cellular environments is often limited due to signal-loss in, and misalignment of the subtomograms. In contrast, single-particle cryo-electron microscopy (SP-cryo-EM) routinely reaches near-atomic resolution of isolated complexes. We have developed a method called "TomographY-Guided 3D REconstruction of Subcellular Structures" (TYGRESS) that is a hybrid of cryo-ET and SP-cryo-EM, and is able to achieve close-to-nanometer resolution of complexes inside crowded cellular environments. TYGRESS combines the advantages of SP-cryo-EM (images with good signal-to-noise ratio/contrast and minimal radiation damage) and subtomogram averaging (3D-alignment of macromolecules in a complex sample). Using TYGRESS, we determined the structure of the intact ciliary axoneme with up to 12 Å resolution. These results reveal many structural details that were not visible by cryo-ET. TYGRESS is generally applicable to cellular complexes that are amenable to subtomogram averaging, bringing us a step closer to (pseudo-)atomic models of cells.

*Correspondence to: Daniela Nicastro, Phone: (++ 1) 214 648 3925; Fax: (++ 1) 214 648 7491; daniela.nicastro@utsouthwestern.edu.

Author contributions

D.N. conceived the study and designed experiments. Z.S. and X.F. programmed, K.S. collected data and processed the data with Z.S.. N.G. contributed significant scientific and technical insights throughout the project. Z.S., K.S., X.L., N.G., and D.N. wrote the manuscript. All authors contributed to discussions and revisions of the manuscript.

Competing interests: The authors declare no competing interests.

Due to recent hardware and image processing advances, single-particle (SP-) cryo-EM can produce three-dimensional (3D) reconstructions of purified, native proteins and macromolecular complexes (from ~50 kDa to several MDa size) with near-atomic detail, i.e. with a resolution of 3 Å or better[1–4]. Even single-particle cryo-ET of relatively thin (<100 nm) samples containing isolated complexes[5], and of viruses with a high abundance of capsomers[6, 7] has reached sub-nanometer resolution. However, relatively thick (>100 nm) and complex cellular samples are not presently amenable to structural study by SP-cryo-EM. The reason is that for unambiguous particle picking and accurate particle alignment, SP-cryo-EM usually requires the particles to be purified, structurally relatively homogeneous, and distributed in a thin monolayer that avoids superposition of particles in the cryo-EM projection images[8].

Unlike other ultrastructural methods, cryo-ET can be used to 3D-reconstruct and visualize pleomorphic structures, such as intact cells and organelles *in situ*. In addition, identical repeating components in the reconstructed tomograms, such as axonemal repeats in cilia or chemoreceptors in bacterial membranes, can be resolved in molecular detail using subtomogram averaging, which increases the signal-to-noise ratio and thus resolution of the reconstruction[9–12]. However, the resolution of cellular cryo-ET and subtomogram averaging is ultimately limited by the need to balance several irreconcilable factors (Supplementary Table 1). For example, a higher electron dose improves the signal-to-noise ratio of the tilt images, increasing accuracy of image alignment and correction of the contrast transfer function (CTF), with positive effects on resolution. On the other hand, a higher electron dose also leads to more structural degradation by radiation damage, limiting useful high-resolution signal to the early exposures in a tomogram. In contrast to thin “single particle-type” samples, the signal in tomograms of cellular samples is degraded by: a) increased inelastic electron scattering due to the large thickness of cellular samples, with the effective thickness increasing by $1/\cos(\alpha)$ with tilt angle α; b) incomplete sampling of the reconstruction in Fourier space beyond a given resolution (Crowther criterion: $m = \pi * D/d$, with number of tilt images m, sample thickness D, and resolution d)[13]; c) beam-induced motion and electrostatic charging affecting images of tilted samples more severely; and d) the initial fast, not fully correctable motion in exposures is reiterated with every new exposure in a tilt series[14]. Some efforts have been made to optimize these factors to achieve higher resolution with subtomogram averaging, such as “constrained single-particle cryo-electron tomography” that uses constrained projection-matching refinement procedures[5, 15, 16], and dose-symmetric tilt-schemes combined with exposure filtering to more efficiently use the high-resolution information from early exposure images that contain less radiation damage[17, 18]. However, only averaging subtomograms of relatively thin and uncrowded samples produces nanometer (or better) resolution[5–7]. Subcellular samples are usually more crowded and thicker than these samples. It is therefore difficult to process their micrographs, and novel strategies are required to push the resolution of *in situ* imaging to close the gap to high-resolution structure determination methods.

Results

TYGRESS - a hybrid method for *in situ* structural studies

Here we describe "TomographY-Guided 3D REconstruction of Subcellular Structures" (TYGRESS) (Fig. 1 and Supplementary Text), a hybrid method for resolving structures *in situ* in crowded cellular environments with higher resolution than was previously possible using cryo-ET and subtomogram averaging. TYGRESS is essentially a single-particle reconstruction from untilted high-dose (HD) images recorded with an electron dose typical for SP-cryo-EM (30–60 e/A^2), which is 10–60 times higher than the electron dose used for individual low-dose (LD) images of a tilt series (Fig. 1a). The HD images therefore contain optimally preserved high-resolution signal by using single exposures of untilted specimens. The SP-cryo-EM reconstruction of protein assemblies in their complex cellular context is made possible by providing additional 3D information for particle picking and initial particle alignment from the cryo-ET reconstruction and subsequent subtomogram averaging that is performed on the same specimen area where a HD image is recorded (Fig. 1b,c).

Briefly, the TYGRESS workflow includes: (1) for each sample area, two datasets are acquired, an HD image at 0° followed by a typical cryo-ET tilt-series (Fig. 1a); (2) the cryo-ET are reconstructed, followed by subtomogram averaging of the particles of interest (Fig. 1b); (3) the information of the 3D particle position in the tomogram is projected onto the 2D HD image for particle picking (Fig. 1c and Supplementary Fig. 1), and the subtomogram angles for each particle are applied for initial particle alignment (Fig. 1c); finally (4) the particles extracted from the HD images are further processed, which includes constrained single particle-type alignment, refinement for sub-averaged particles, and CTF- and B-factor correction to generate the final reconstruction (Fig. 1d and Supplementary Fig. 2), whereas the cryo-ET data themselves are not included in the final TYGRESS average. There are multiple advantages of TYGRESS over cryo-ET/subtomogram averaging, including previously published strategies for cryo-ET resolution improvement, which in sum should lead to a considerable resolution improvement: a) the higher electron dose of the HD image substantially improves the signal-to-noise ratio and thus the reliability of SP-cryo-EM refinement strategies and CTF correction; b) HD images are recorded with an electron dose of ~30 e/Å^2 (at 300 kV) and therefore are affected far less by radiation damage than images used in regular cryo-ET/subtomogram averages, which suffer accumulated doses of up to ~100 e/Å^2); and c) the image quality of HD images is not degraded by sample tilting and multiple exposures.

TYGRESS - validation using the ciliary axoneme

For validation, we applied TYGRESS to the intact ciliary axoneme from the multiciliated protist *Tetrahymena thermophila*, a complex cell organelle that has been extensively studied by cryo-ET and subtomogram averaging. The axoneme is the evolutionarily conserved microtubule core of cilia and flagella, with a canonical array of nine outer doublet microtubules (DMTs) surrounding two central single microtubules that form the scaffold for more than 400 different associated proteins (Supplementary Fig. 3)[19]. Each DMT is composed of 96-nm repeat units, which can be treated as particles for subtomogram averaging. In the currently more than 30 published cryo-ET studies of the >200 nm thick

ciliary axonemes, the achieved resolution ranged from ~3–4 nm resolution (FSC 0.5 criterion)[9, 20–24], with the best resolution of 2.5 nm (FSC 0.5 criterion) being achieved using Volta-Phase-Plate and K2 data[11]. These studies provided insights into the functional organization of axonemes, the mechanisms of dyneins and cilia motility, and ciliary dysfunction in human diseases[9, 20, 22]. However, the resolution of cryo-ET is still insufficient to characterize protein-protein interactions and conformational changes that underlie cellular processes with molecular detail.

We applied TYGRESS to intact *Tetrahymena* axonemes by acquiring 99 HD images of 152 axonemes, each followed by a typical cryo-ET tilt-series, and picking 18,857 particles for averaging. After constrained alignment of the picked particles from the HD image, we obtained an averaged 3D structure of the 96-nm axonemal repeat *in situ* with a resolution of up to 12 Å (FSC 0.143 criterion), a considerable improvement over the best previous published resolution (Figs. 2–4; Supplementary Figs. 4–6; Supplementary Video 1). Many molecular complexes and *in situ* structural details previously unseen were revealed, including the 96-nm axonemal ruler and other ruler-like structures (Fig. 3a–e and Supplementary Fig. 4), individual nexin-dynein regulatory complex (N-DRC) components (Fig. 3f and Supplementary Fig. 4), and microtubule inner proteins (MIPs) (Fig. 4; Supplementary Figs. 5 and 6). These data will shed light on the molecular mechanisms of ciliary assembly and the roles played by individual axonemal proteins in normal ciliary function.

TYGRESS reconstruction resolution improvement

The use of direct electron detectors (e.g., K2 camera) is a key reason for the recent success and resolution improvement of SP-cryo-EM[8]. However, using cryo-ET in combination with a K2 camera for subtomogram averaging of the 96-nm repeat in intact ciliary axonemes resulted only in a small resolution improvement (27.5 Å, FSC 0.5 criterion) over the cryo-ET average using a CCD camera (30 Å)[20] (Fig. 2a–d). In contrast, using TYGRESS in combination with a K2 camera, we reconstructed the 96-nm repeat at up to 12 Å resolution (FSC 0.143 criterion, measured at the DMT regions of the axoneme) (Fig. 2a–d). This is the highest resolution of the intact axoneme structure reported to date. Only SP-cryo-EM reconstructions of isolated and dialyzed DMTs have achieved a better resolution[25], with the caveat that all external and some internal DMT structures were lost during the DMT isolation procedure. The resolution of the TYGRESS reconstruction allows individual tubulin monomers of the DMT walls can be distinguished (Fig. 2b, right panel), facilitating generation of a pseudo-atomic model by fitting the tubulin dimer model derived from the high-resolution SP-cryo-EM map of tubulin (EMDB: EMD-6353)[26] into the DMT structure. By subtracting the pseudo-atomic DMT model from the actual DMT density we calculated a structural difference map that revealed the densities of a large amount of accessory proteins and complexes (at least 20 MIPs and 2 previously unreported MAPs) that are assembled on the DMT scaffold (Fig. 2e).

The DMT is a highly repetitive structure, and by increasing the number of averaged particles to 112,386 by averaging the 16-nm repeating units of the DMT wall and several MIP structures, we were able to further improved the resolution from 12 Å to 10.6 Å (Fig. 2d). At

this resolution, the pseudo-atomic models of individual ciliary proteins and/or domains could be reliably fitted into the structure (Fig. 2 f,g).

Molecular rulers and ruler-like structures facilitate MAP docking

Our resolution-improved structure of the intact axoneme enabled the detailed visualization of known and previously uncharacterized MAP structures. Several of these MAPs are filamentous and appear to be adaptors for binding of other accessory structures to the outer surface of DMTs (Fig. 3a–e and Supplementary Fig. 4a). A previous study identified the FAP59/172 complex as a "96-nm axonemal ruler" (AR) that is required for proper attachment of radial spokes RS1 and RS2, as well as inner dynein arms to the DMT[23]. The ruler components FAP59 and FAP172 were crudely localized using genetics and cryo-ET of cloneable tags, but the FAP59/172 complex itself could not be visualized[23]. In the TYGRESS average, the filamentous structure of the FAP59/172 complex was clearly observed running along the DMTs in the outer cleft between protofilaments A2 and A3, with two globular domains near the bases of RS1 and RS2 (AR in Fig. 3a–d and Supplementary Fig. 4a). Several axonemal complexes essential for ciliary motility seem to directly connect to the FAP59/172 filament, including RSs 1–3, N-DRC, I1 tether/tether head (I1 T/TH), and some of the inner dyneins (Fig. 3d and Supplementary Video 2). In contrast, inner dyneins *a* and *c* are attached to the front-prong of RS1 and RS2, respectively. This is consistent with the previous study that demonstrated that the FAP59/172 complex is critical for docking of these structures[23].

We resolved a second long filamentous structure, here termed "inner dynein arm (IDA) ruler-like structure (IA-R)", running along the outer surface of the DMT in the cleft between protofilaments A4 and A5 (Fig. 3b,c and Supplementary Fig. 4a). Its proximal terminus starts at a density connected with I1 between RS1 and RS2, and connects to the tail of IDA a, d, and g (Fig. 3e). The direct connections between IA-R and protofilament A4 with 4-nm periodicity are clearly resolved (Fig. 3e, white arrows). This periodic connection between IA-R and protofilament A4 is not observed in the region of the I1 dynein complex (Fig. 3e). Therefore, the IA-R may play a similar role as the 96-nm AR by determining the periodic docking of several IDAs. To date, the molecular composition of the IA-R has not been determined.

The outer dynein arms (ODAs) attach to the outer surface of DMTs with 24 nm periodicity, but the molecular mechanism underlying this regular docking remains unclear. The ODA docking complex (ODA-DC) has been proposed to be responsible for the 24-nm periodicity of ODAs[27]. However, purified *Chlamydomonas* ODAs can assemble with proper periodicity onto DMTs that were isolated from *oda3* mutants lacking the ODA-DC[28] suggesting that ODA-DC does not determine ODA periodicity. The TYGRESS average reveals a 24 nm-long filamentous structure, here tentatively termed "ODA ruler-like structure (OA-R)" that runs along the outside cleft between protofilaments A7 and A8 (Fig. 3a,c and Supplementary Fig. 4a) and has a globular density at the docking site of the ODAs (Fig. 3d).

N-DRC base plate and linker base organization

The N-DRC is connected to neighboring DMTs[9, 29, 30], which is critical for restricting and thus transforming interdoublet sliding into ciliary bending motion[29, 31]. The N-DRC is separated into two major regions, the base plate that is required for the N-DRC binding to the DMT, and the linker region that connects to the neighboring DMT (Fig. 3f), and which is critical for both axoneme integrity and ciliary motility[32]. In contrast to previous cryo-ET studies that observed the N-DRC base plate as a single rod-shaped density[33], in the TYGRESS reconstruction three N-DRC subunits were well-resolved as three long filamentous structures that are twisted around each other (shown in purple, yellow, and dark green in Fig. 3f). Twisted filaments is a common feature of cellular filaments with considerable stability and tensile strength, such as F-actin and intermediate filaments[34, 35]. We proposed that these filamentous structures are DRC1, 2, and 4, subunits that have previously been localized to the N-DRC base plate[29], and that are predicted to be enriched in coiled-coil domains[36].

Our structure revealed two similar N-DRC filaments (yellow and dark green in Fig. 3f) that reach from the inner junction between the A- and B-tubule, to the proximal lobe of the N-DRC, and directly connect to the 96-nm AR and the DMT. This suggests a role of these subunits in the assembly and docking of the N-DRC. We propose that these filaments are DRC1 and DRC2, because it has been shown that their absence in *pf3* and *ida6* mutant axonemes causes the loss of the entire base plate[29, 36–38]. In contrast, the shorter filament with associated globular domain (purple in Fig. 3f) binds on top of DRC1 and 2, and thus is likely not essential for base plate assembly, but seems to directly connect to the linker arm L1 (light green in Fig. 3f). These structural features and previously described mutant phenotypes are consistent with the short base plate filament being DRC4, which connects to DRC3 in the L1 arm[33].

Inner junction organization

The inner junction (IJ) between the A- and B-tubules (also called the “B-11th density”[39]), was previously shown to be a non-tubulin connection between protofilaments A1 and B10[40]. A recent cryo-ET study of IJ mutants showed that the IJ is composed of two proteins, FAP20 (22 kDa) and PACRG (34 kDa), which alternate along the DMT length[41]. In latter study, we improved the resolution of axonemal averages from ~3 nm to ~2.5 nm due to hardware advances (e.g. contrast increase by phase plate imaging). However, even at ~2.5 nm resolution the densities of the two IJ proteins appeared globular and structurally indistinguishable. In contrast, in the higher resolution TYGRESS reconstruction we can clearly distinguish structural features that suggest two periodicities (Supplementary Fig. 4b–g): FAP20 (round density with a small neck; gray arrowheads in Supplementary Fig. 4c,d) and PACRG (oval-shaped density with a long filamentous extension; black arrowheads in Supplementary Fig. 4c,d) alternate and have an 8 nm periodicity, whereas the connections between the IJ proteins and protofilament A13 have a 16 nm periodicity (Supplementary Fig. 4c,d). Our data revealed an additional density extending from the N-DRC baseplate (Supplementary Fig. 4f, purple arrowhead) to one of the FAP20 subunits next to the previously reported hole on the IJ (Supplementary Fig. 4c,f, white arrowheads), suggesting

that one PACRG subunit is missing from each 96-nm repeat due to interference with the C-terminal domains of DRC1 and 2.

Many MIPs binds to the inside of the A- and B-tubule walls

MIPs were discovered as structures that bind periodically to the inner surface of the ciliary DMT walls[9]. Although MIPs are proposed increase the stability of DMTs, functional studies have not been possible because MIP proteins have not yet been identified. A recent SP-cryo-EM study of isolated DMTs has visualized the ciliary MIPs[25] but suffered from two limitations: a) the DMTs adopt a preferred orientation in the thin ice layer on the EM grids, which has previously been observed[42] and resulted in anisotropic resolution (similar to a missing wedge in cryo-ET); and b) the DMT isolation procedure involved high salt extraction and dialysis to remove MAPs from the outside surface of the DMT, which also resulted in the dissociation of other structures, such as the inner junction proteins[25].

In the TYGRESS reconstruction, the MIPs were well resolved and could be grouped into 20 discrete densities (MIPs 1–20) (Fig. 4; Supplementary Figs. 5 and 6). MIPs 1–6, which have been previously observed[9, 43, 44], were revealed in greater structural detail, distinguishing MIP substructures. For example, the three substructures of MIP2 (MIP2a, b, and c) previously appeared as three similar globular densities by cryo-ET (Fig. 2b, left panel). In contrast, the TYGRESS average clearly resolves structural differences between MIP2a, b, and c (Fig. 2b, right panel; Fig. 4a;Supplementary Fig. 5). Thus, the periodicity of the MIP2 proteins has to be corrected from the previously reported 16 nm to the here observed 48 nm periodicity. Similarly, MIP6, which was reported as a continuous structure spanning protofilaments A1–3, is now resolved as four discrete substructures, MIP6a-d (Fig. 4b and Supplementary Fig. 5).

MIPs 7–20 were not visualized by previous cryo-ET and subtomogram averaging studies but are now resolved by TYGRESS of intact ciliary axonemes (Fig. 4c; Supplementary Figs. 5 and 6), and by SP-cryo-EM of isolated DMTs[25]. The architecture resolved by TYGRESS suggests that the MIPs form a complex network that could increase the stability of the DMTs[44], for example by strengthening the usually relatively weak lateral protofilament-to-protofilament interactions of microtubules[45]. The axoneme forms a scaffold in cilia that serves as a persistent platform for the attachment of hundreds of accessory proteins, making the stabilizing MIP network essential for maintaining DMT integrity under the considerable mechanical stress during ciliary beating. All of the here described MAPs, the inner junction and some of the MIPs were completely missing from the high-resolution SP-cryo-EM structure of isolated DMTs[25], highlighting the critical need for a method like TYGRESS that can visualize cellular structures *in situ* at high resolution.

Discussion

In summary, our results provide a deeper understanding of the functional organization of the DMTs and ciliary axoneme (Fig. 4d,e), and they demonstrate that TYGRESS can resolve macromolecular complexes at near nanometer resolution while they are maintained *in situ*, i.e. in their cellular context. Here, we have used TYGRESS to reconstruct the 96-nm axonemal repeat at 12 Å. We expect the resolution to improve further by using: Energy-

filtered data recorded on more stable cryo-stages; patch-based motion correction for the alignment of direct electron detector movie frames (MotionCor2)[46]; and CTF correction that take into account the variable z-height of particles within the sample[47]. Furthermore, given larger datasets, single-particle classification could be used to calculate more homogeneous class averages, to retrieve ultrastructural differences that are biologically meaningful. Generally, the TYGRESS method should improve the resolution of cellular 3D reconstructions that are amenable to subtomogram averaging, especially in cases where sample thickness and radiation damage are the main resolution-limiting factors. TYGRESS is ultimately a SP-reconstruction method and thus will continue to benefit from the same future advances that improve SP-cryo-EM of isolated proteins complexes. However, similar to SP-cryo-EM, preferred orientation of structures, e.g. focal adhesion complexes[48] that are always oriented parallel to the EM grid, cannot be overcome by TYGRESS unless tilted HD images are included in the reconstruction. An added advantage of the cryo-ET and subtomogram averages is that they can be used to classify structurally heterogeneous complexes in 3D before calculating TYGRESS class averages. One current challenge with TYGRESS is that data acquisition and image processing is time-consuming. However, future developments of high-throughput tilt-series acquisition, possibly in minutes using continuous camera exposure while the sample is tilted in quick increments with highly eucentric TEM specimen stages, and continued improvements to automate (batch-) tilt series alignments and tomogram reconstructions, could considerably decrease the time needed for TYGRESS data acquisition and processing.

Methods

Cryo-sample preparation

Wild-type axonemes were isolated from *Tetrahymena thermophila* strain CU428, as previously described[22]. Briefly, cilia were detached from cells using the pH-shock method[51] and purified by centrifugation at 2,400 *g*, 4 °C, for 10 min (twice). Purified cilia were demembranated using 1% IGEPAL CA-630 (Sigma-Aldrich) in HMEEK buffer (30 mM HEPES, pH 7.4, 5 mM $MgSO_4$, 1 mM EGTA, 0.1 mM EDTA, and 25 mM KCl) and axonemes were collected by centrifugation at 10,000 *g*, 4 °C, for 10 min. The axoneme pellet was carefully resuspended in HMEEK buffer and cryo-samples were prepared as previously described[21]. Briefly, Quantifoil grids (Quantifoil MicroTools GmbH, Germany) were glow discharged for 30 s at −40 mA before use, coated with 10 nm colloidal gold (Sigma–Aldrich), and loaded on a plunge freezing device. Then, 3 μl of axoneme sample and 1 μl of a five-fold-concentrated 10-nm BSA-coated, colloidal gold solution[52] were added to the grid and mixed. The grid was blotted with filter paper for 1.5–2.5 s and immediately frozen by plunging into liquid ethane. The vitrified samples were then stored in liquid nitrogen until examination by electron microscopy.

Image acquisition

The frozen grid was mounted in a cryo-holder (Gatan Inc., Pleasanton, CA) and imaged on a Tecnai F30 transmission electron microscope (FEI, Inc., Hillsboro, OR) equipped with a field emission gun and operated at 300 keV. The data were collected under low-dose conditions using the SerialEM software[53]. For each intact axoneme, two sets of data were

collected using a K2 direct electron detector (Gatan Inc., Pleasanton, CA) at a magnification of 9400x; first, a movie stack (80 frames) was collected at 0° with a total electron dose of ~30 e/Å^2 (HD image) at varying defocuses of −1.5 to −3 μm in the K2 super-resolution mode; second, a typical tilt series with an accumulated electron dose of ~100 e/Å^2 (LD images) was recorded in the K2 counting mode at a defocus of −8 μm using a bidirectional tilt scheme, i.e. a continuous series of tilt images was recorded from 0° to −64° with 2° increments, followed by a second series from 2° to 64°. At each tilt angle, a movie stack (5 frames) with an exposure time of 2 seconds and an electron dose of 1.5 e/Å^2 was recorded. The resulting pixel sizes of the 0° HD image and the LD images were 0.2112 nm and 0.4224 nm, respectively. The parameters used for data collection are summarized in Supplementary Table 2.

Image processing

Full-frame motion correction of the movie stacks was performed using IMOD scripts[54]. Then, both the HD image and LD images were aligned using fiducial markers. The LD images alone were further reconstructed into a 3D tomogram by weighted back-projection using the IMOD software package. Subtomograms containing the 96-nm axonemal repeats were extracted from the tomograms, aligned, and averaged using PEET[9]. The HD images were used to reconstruct high resolution structures of the 96-nm axonemal repeats with the TYGRESS method developed in this study (see supplementary text for details). FREALIGN[55] was used for the final reconstructions as part of TYGRESS. CTFFIND3 (ref. 56) was used to detect defocus values; the power spectra of about 200 patches with dimension of 256 × 256 pixels were averaged to generate the CTF. BFACTOR[57] was used to sharpen and filter the final reconstruction. The pseudo-atomic model of MIP3a/FAP52 was generated and calculated from the protein sequence using the ExPASy online tool, SWISS-MODEL[58]. UCSF Chimera[59] was used for 3D visualization and high-resolution structure (e.g. x-ray, pseudo-atomic model) fitting.

Resolution measurement

The resolution of the TYGRESS reconstruction was measured using the FSC[49]. Briefly, the dataset was divided into two halves using even and odd indexes at the outset; initial reference models for each dataset were generated using its corresponded subtomogram averaged structure; then the two halves were aligned and reconstructed independently and the FSC between the two reconstructions was calculated.

TYGRESS image processing

TYGRESS is essentially a single-particle reconstruction method using coordinate information provided by cryo-ET to enable particle picking (Fig. 1). During imaging, two datasets were acquired for each region of interest: a 2D image (HD image) at 0° tilt for the final TYGRESS reconstruction using an electron dose typical for conventional SP-cryo-EM, and a traditional low-dose tilt series (LD images) that was used for positional information. To minimize the effects of radiation damage in the final reconstruction, the HD image was recorded prior to the LD images (Fig. 1a).

Alignment of the combined tilt series and tomogram reconstruction with subtomogram averaging

During image processing, each HD image was inserted into the corresponding tilt series at the angle corresponding to where the HD image was taken (for example, an HD image recorded at 0° was inserted just before the LD image at 0°) using the command 'newstack' in IMOD, resulting in a "combined tilt series". The combination of HD and LD images ensured a common reference frame for the later steps in the TYGRESS procedure. The combined tilt series was then aligned based on the 10-nm gold fiducial markers using the IMOD software package. However, only the LD images were used to calculate a tomogram after alignment, and then subtomogram averaging was performed using PEET (Fig. 1b). Here, the 96-nm repeat unit of the axoneme can be readily identified based upon structural features such as the doublet microtubule (MT) walls and the RSs, which allowed us to pick particles of 240 × 240 × 240 pixels (240 × 0.4224 nm = 101 nm) from the noisy raw tomograms. Subtomogram averaging was performed using the raw tomogram and a reference, which was constantly updated using the average structure of the last iteration. In total, 19,830 particles were picked from 152 axoneme tomograms and aligned in PEET for subtomogram averaging.

The HD image was excluded for tomogram reconstruction and subtomogram averaging to avoid (1) reconstruction artifacts due to uneven weighting of the HD and LD images in the tomogram, and (2) alignment bias in the initial reconstruction calculated from the HD image.

Retrieval of coordinates and orientations for picking the particle in 2D on the HD image

Because the HD image was aligned together with the LD images during tomographic reconstruction, we could retrieve the 2D HD image particle coordinates and orientations that correspond to the subtomogram particles in the 3D tomogram. The final coordinates $\{x, y\}$ and orientations $\{\alpha, \beta, \gamma\}$ for each 2D HD image particle are given as:

$$N^{sp}_{(x,\,y)} = N^{imod}_{(\delta x,\,\delta y)} + Proj_{(xyplane)}\left[F^{-1}_{imod(C)} N^{peet}_{(x,\,y,\,z)}\right] \tag{1}$$

$$N^{sp}_{(\alpha,\,\beta,\,\gamma)} = N^{imod}_{(\delta\alpha,\,\delta\beta,\,\delta\gamma)} + F^{-1}_{imod(O)} N^{peet}_{(\alpha,\,\beta,\,\gamma)} \tag{2}$$

Where, $(\delta x, \delta y)$ and $(\delta a, \delta\beta, \delta\gamma)$ are the HD image shift and rotation from the fiducial gold alignment of the combined tilt series; $N^{peet}_{(x,\,y,\,z)}$ and $N^{peet}_{(\alpha,\,\beta,\,\gamma)}$ are the 3D particle coordinates and orientations in the tomogram after PEET alignment; and $F^{-1}_{imod(C)}$ and $F^{-1}_{imod(O)}$ represent the inverse transformations for coordinates and orientations of particles in the HD image, which shares the same parameters as the 0° tilt LD image of the tomogram. $Proj_{(xyplane)}$ converts the 3D coordinates to 2D coordinates in the HD image.

2D Particle picking from HD image

The command 'EXCISE' from the IMOD package was used to extract particles from the HD image according to the coordinates determined from the tomogram. In this work, the particle

box size was set to 320 × 320 pixels, which corresponds to the size of the 3D volume extracted from the tomogram. This size (320 × 0.4224 = 135 nm) is sufficient to cover an entire 96-nm axonemal repeat. An example of how TYGRESS successfully identified the particle center from the overlapping projection images of an axoneme is shown in Supplementary Fig. 1.

Constrained alignment and reconstruction of the 2D HD particles

Before the 3D reconstruction of the particle of interest can be calculated using all particle images that were extracted from the 2D HD images, the particle images – which represent projections of the particle in different orientations – have to be aligned. A variety of algorithms and image processing methods have been developed to facilitate 2D and 3D particle alignment[8, 60], including approaches specifically developed to improve alignment in cases where structural information overlaps in the experimental 2D images. Latter methods usually pre-process the data to reduce negative effects of the "background" information on the accuracy of the target particle alignment, for example by using the high spatial-frequency information and a whitening filter to detect proteins in crowded cellular environments[61], or by "signal subtraction" from the experimental particle images prior to performing (focused) alignments. The "signal subtraction" approach has been used to reconstruct membrane proteins embedded in liposomes[62], proteins decorating microtubules[63], and to dissect continuous structural heterogeneity in cryo-EM single-particle data using multi-body refinement[64].

Here we developed an alignment refinement algorithm that is tailored towards samples containing many copies of the particle of interest that might also overlap in the 2D HD images, such as in the cylindrically organized axonemal repeat, studied here, or other samples previously studied by subtomogram averaging (e.g. COPI and II vesicle coats[65, 66], HIV envelope glycoproteins[6, 67], the tubular contractile injection systems in bacteria[68] or crowded nucleosomes in nuclei[69]). However, depending on the nature of the sample, TYGRESS can also be combined with other existing (e.g. whitening filter[61]) or newly developed alignment refinement approaches (as described below). The alignment approach developed here combines the information provided by the previous subtomogram averaging step and elements from iterative reprojection-based alignment[16]. Specifically, we generate and iteratively refine an alignment reference for each to-be-aligned particle that both reprojects the latest 3D particle average in the position and orientation of the target particle, and sums the reprojections of all particles that contribute to the overlapping information in the experimental 2D HD image for the target particle to best match the reference with the experimental 2D particle image. Initial position and angular orientations of the particles (α, β, γ) are provided by the subtomogram averaging step, and the parameters are then iteratively refined over several alignment rounds.

The 2D HD particle image alignment is performed as "constrained alignment" because, in the 2D HD images, the particle information is convoluted by information from the complex environment that surrounds the particle and thus overlaps the particle information in the 2D HD projection image. Cross-correlation alignment between the 2D HD particle image and 2D reference images that are generated by reprojecting a 3D reference using the full euler

angle space could cause “false” cross-correlation peaks with background features and thus result in misalignment of the target particle. In contrast, the alignment during the subtomogram averaging step can be performed without constraining the angular search range, because the 3D reconstructed particles in the raw tomograms are not convoluted by overlapping background information that could generate misalignment. Thus, an advantage of TYGRESS is that not only the subtomogram average itself can be used as initial reference, but also the subtomogram alignment parameters can be used as good initial alignment that only requires small refinements driven by the high-frequency (high-resolution) information that is present in the 2D HD particle images but is degraded in the lower resolution subtomogram volumes due to radiation damage. Thus for the “constrained alignment” of the 2D HD particle images the parameter changes are limited to a user-defined range around the initial subtomogram-averaging alignment; for example, here, the initial range for allowed alignment changes was set to ±4 nm positional and ±5 degrees angular changes from the subtomogram averaging alignment.

Using the coordinates retrieved from the subtomogram averaging step, we calculated the position of each target particle and of “neighboring” particles that overlap in the 2D HD image with the target particle (the radius for how many particles to include is user-defined in the TYGRESS input file). For the constrained cross-correlation alignment of each target particle picked from the 2D HD images, a set of 2D reference images was generated by performing the following steps: 1) For the target and all-to-be-included “neighboring” particles, 2D re-projection images were generated from the latest 3D reference model – initially this is the subtomogram average. For the re-projection of the “neighboring” particles the angles from the subtomogram averaging were used. For the target particle, a set of re-projections was calculated that varied by a user-defined range (1° steps) around the subtomogram averaging angles. 2) Each target-particle re-projection was then combined with the re-projections of the “neighboring” particles using the relative positions between the included particles to generate the correlating 2D reference image. This resulted in a target-particle-specific set of 2D reference images that varied only slightly in the orientation of the target particle. In a next step, the 2D HD particle image was then cross-correlated to each 2D reference from the set and the match with the highest cross-correlation coefficient was used to update the alignment parameters of the target particle. This was performed for each particle picked from the 2D HD images.

The constrained alignment is iterative in nature, with the first iteration refining the subtomogram averaging positional and angular parameters (x, y shifts and angles) for each target particle. For the next iteration of the constrained alignment, the refined alignment parameters for each particle are used to generate updated reference models for each target particle and the search constraints are tightened, i.e. here, to 1 nm shift and 2 degree angular deviation from the parameters obtained in the previous round. After several iterations, a final set of parameters for each target particle is generated and used for the 3D reconstruction of the particle of interest.

CTF estimation of the HD images, as well as the first round of constrained alignment, were performed using movie averages that contained all frames (e.g. frames 1–80 in this work) (Supplementary Fig. 2). To account for local beam-induced sample motion that was not

corrected by the whole-frame alignment in IMOD, sub-frame averages were calculated using frames 3–21, 22–40, 41–59, and 60–78 (the initial two frames were excluded due to in-frame blurring), and the following rounds of constrained alignment was done using each of these sub-frames. The aligned particles from these sub-frames were then recombined to calculate the 3D reconstruction (Fig. 1). The latter step could potentially be avoided if motion-correction is performed on image patches rather than global whole-frame alignments. Moreover, to improve the alignment of substructures (like dynein arms within the large 96-nm axonemal repeat), we occasionally focused the alignment on these by masking neighboring densities.

The alignment method we describe here for the 2D HD particle images, using composed 2D re-projected references, is well-suited for samples in which the tomographic volumes contain many particle copies, since their densities can be summed to generate references that account for parts of the overlapping densities in the experimental 2D HD images. Therefore, samples that would benefit most from this algorithm include, for example, cytoskeletal assemblies with multiple repeats (e.g. muscle sarcomeres, actin networks), viruses, and vesicle-bound proteins. However, users can also combine other existing or newly developed alignment methods with TYGRESS. For example, in cytosolic environments with non-averageable background information surrounding the particles of interest, alignment methods which involve subtracting background or applying a whitening filter to the experimental 2D HD images may be advantageous[61, 62, 64]. To combine alternate alignment methods with TYGRESS, users should skip step # 5.5 in the step-by-step protocol (step # 3 in the TYGRESS GUI) and instead use the initial alignment parameters from the subtomogram averaging that are provided as output from step # 5.4 (step # 2 in the TYGRESS GUI) in the file [*.par]. After performing alignment refinement externally, the users can add the refined alignment parameters into the [*.par] file and replace the old [*.par] file before continuing with step # 5.6 (step # 4 in the TYGRESS GUI) to calculate the final reconstruction (the file format for [*.par] is provided as template in folder / example/combined_PEET/HD_particles/WT_20120914_S1/ after TYGRESS installation).

Similar to subtomogram averages of cellular samples, the quality and resolution of TYGRESS reconstructions of subcellular structures could ultimately be limited by the background added by overlapping unrelated structures within crowded environments. Although randomly distributed unrelated structures will be averaged out, resulting in a smooth background, the absolute contrast between the averaged particle and the background is smaller compared to the contrast achievable in SP-cryo-EM between the isolated proteins and the surrounding aqueous buffer.

Statistics and Reproducibility

All samples used in this work were from two independent sample preparations. In total, 99 HD images, each followed by a typical cryo-ET tilt-series (with 1–2 axonemes per series) were collected during 11 cryo-EM data acquisition sessions, resulting in tomographic reconstructions of 152 axonemes. 19,830 particles were picked for cryo-ET/subtomogram averaging of the 96-nm axonemal repeat. 18,857 (112,386) particles picked from HD images

were used to generate the TYGRESS average of the 96-nm axonemal (16-nm microtubule) repeat.

Reporting Summary—Further information on research design is available in the *Nature Research Reporting Summary* linked to this article.

Data availability—The TYGRESS reconstructions have been deposited in the Electron Microscopy Data Bank (EMDB) under accession code EMD-9023. All other data that support the findings of this study are available in the manuscript or the supplementary files or from the corresponding author upon request.

Code availability—TYGRESS source code and documentation are available on Code Ocean (Link will be available to readers upon publication). The TYGRESS program is also available at www.tygress.org

Supplementary Material

Refer to Web version on PubMed Central for supplementary material.

Acknowledgements

We thank Chen Xu for training and maintaining the electron microscopy facility at Brandeis University. We thank John Heumann and David Mastronarde (Univ. of Colorado at Boulder) for technical advising concerning cryo-ET and subtomogram averaging, and Alexis Rohou (Janelia Research Campus) and Stephen C. Harrison (Harvard Medical School) for helpful discussions. We thank Thomas Ni and Justine Pinskey (UT Southwestern) for critically reading the manuscript, and Rui Zhang at Washington University for providing the EM structure of tubulin dimer for docking. This work was supported by funding from the National Institutes of Health (R01 GM111506 to D.N.). N.G. is an investigator of the Howard Hughes Medical Institute.

Abbreviations

cryo-ET	Cryo-electron tomography
CTF	Contrast transfer function
DMTs	Doublet microtubules
IDAs	Inner dynein arms
I1 T/TH	I1 tether/tether head
IJ	Inner junction
MAPs	Microtubule-associated proteins
MIPs	Microtubule inner proteins
N-DRC	Nexin-dynein regulatory complex
ODAs	Outer dynein arms
PFs	Protofilaments

RSs	Radial spokes
SP-cryo-EM	Single-particle cryo-EM
TYGRESS	TomographY-Guided 3D REconstruction of Subcellular Structures

References

1. Bai XC, McMullan G, Scheres SH, How cryo-EM is revolutionizing structural biology. Trends in biochemical sciences 40, 49–57 (2015). [PubMed: 25544475]
2. Cheng Y, Single-Particle Cryo-EM at Crystallographic Resolution. Cell 161, 450–457 (2015). [PubMed: 25910205]
3. Herzik MA Jr., Wu M, Lander GC, Achieving better-than-3-Å resolution by single-particle cryo-EM at 200 keV. Nature methods 14, 1075–1078 (2017). [PubMed: 28991891]
4. Bartesaghi A, Aguerrebere C, Falconieri V, Banerjee S, Earl LA, Zhu X, Grigorieff N, Milne JLS, Sapiro G, Wu X, Subramaniam S, Atomic Resolution Cryo-EM Structure of beta-Galactosidase. Structure 26, 848–856 e843 (2018). [PubMed: 29754826]
5. Bartesaghi A, Lecumberry F, Sapiro G, Subramaniam S, Protein secondary structure determination by constrained single-particle cryo-electron tomography. Structure 20, 2003–2013 (2012). [PubMed: 23217682]
6. Schur FK, Obr M, Hagen WJ, Wan W, Jakobi AJ, Kirkpatrick JM, Sachse C, Krausslich HG, Briggs JA, An atomic model of HIV-1 capsid-SP1 reveals structures regulating assembly and maturation. Science 353, 506–508 (2016). [PubMed: 27417497]
7. Wan W, Kolesnikova L, Clarke M, Koehler A, Noda T, Becker S, Briggs JAG, Structure and assembly of the Ebola virus nucleocapsid. Nature 551, 394–397 (2017). [PubMed: 29144446]
8. Cheng Y, Grigorieff N, Penczek PA, Walz T, A primer to single-particle cryo-electron microscopy. Cell 161, 438–449 (2015). [PubMed: 25910204]
9. Nicastro D, Schwartz C, Pierson J, Gaudette R, Porter ME, McIntosh JR, The molecular architecture of axonemes revealed by cryoelectron tomography. Science 313, 944–948 (2006). [PubMed: 16917055]
10. Briggs JA, Structural biology in situ--the potential of subtomogram averaging. Current opinion in structural biology 23, 261–267 (2013). [PubMed: 23466038]
11. Fu G, Wang Q, Phan N, Urbanska P, Joachimiak E, Lin J, Wloga D, Nicastro D, The I1 dynein-associated tether and tether head complex is a conserved regulator of ciliary motility. Molecular biology of the cell 29, 1048–1059 (2018). [PubMed: 29514928]
12. Briegel A, Wong ML, Hodges HL, Oikonomou CM, Piasta KN, Harris MJ, Fowler DJ, Thompson LK, Falke JJ, Kiessling LL, Jensen GJ, New insights into bacterial chemoreceptor array structure and assembly from electron cryotomography. Biochemistry 53, 1575–1585 (2014). [PubMed: 24580139]
13. Crowther RA, Derosier DJ, Klug A, The reconstruction of a three-dimensional structure from projections and its application to electron microscopy. Proceedings of the Royal Society of London. Series A 317, 319–340 (1970).
14. Brilot AF, Chen JZ, Cheng A, Pan J, Harrison SC, Potter CS, Carragher B, Henderson R, Grigorieff N, Beam-induced motion of vitrified specimen on holey carbon film. Journal of structural biology 177, 630–637 (2012). [PubMed: 22366277]
15. Himes BA, Zhang P, High resolution in situ structural determination of heterogeneous specimen. BioRxiv, (2017).
16. Yu L, Snapp RR, Ruiz T, Radermacher M, Projection-based volume alignment. Journal of structural biology 182, 93–105 (2013). [PubMed: 23410725]
17. Grant T, Grigorieff N, Measuring the optimal exposure for single particle cryo-EM using a 2.6 A reconstruction of rotavirus VP6. eLife 4, e06980 (2015). [PubMed: 26023829]

18. Hagen WJH, Wan W, Briggs JAG, Implementation of a cryo-electron tomography tilt-scheme optimized for high resolution subtomogram averaging. Journal of structural biology 197, 191–198 (2017). [PubMed: 27313000]
19. Pazour GJ, Agrin N, Leszyk J, Witman GB, Proteomic analysis of a eukaryotic cilium. The Journal of cell biology 170, 103–113 (2005). [PubMed: 15998802]
20. Lin J, Nicastro D, Asymmetric distribution and spatial switching of dynein activity generates ciliary motility. Science 360, (2018).
21. Lin J, Okada K, Raytchev M, Smith MC, Nicastro D, Structural mechanism of the dynein power stroke. Nature cell biology 16, 479–485 (2014). [PubMed: 24727830]
22. Lin J, Yin W, Smith MC, Song K, Leigh MW, Zariwala MA, Knowles MR, Ostrowski LE, Nicastro D, Cryo-electron tomography reveals ciliary defects underlying human RSPH1 primary ciliary dyskinesia. Nature communications 5, 5727 (2014).
23. Oda T, Yanagisawa H, Kamiya R, Kikkawa M, A molecular ruler determines the repeat length in eukaryotic cilia and flagella. Science 346, 857–860 (2014). [PubMed: 25395538]
24. Pigino G, Bui KH, Maheshwari A, Lupetti P, Diener D, Ishikawa T, Cryoelectron tomography of radial spokes in cilia and flagella. The Journal of cell biology 195, 673–687 (2011). [PubMed: 22065640]
25. Ichikawa M, Liu D, Kastritis PL, Basu K, Hsu TC, Yang S, Bui KH, Subnanometre-resolution structure of the doublet microtubule reveals new classes of microtubule-associated proteins. Nature communications 8, 15035 (2017).
26. Zhang R, Alushin GM, Brown A, Nogales E, Mechanistic Origin of Microtubule Dynamic Instability and Its Modulation by EB Proteins. Cell 162, 849–859 (2015). [PubMed: 26234155]
27. Owa M, Furuta A, Usukura J, Arisaka F, King SM, Witman GB, Kamiya R, Wakabayashi K, Cooperative binding of the outer arm-docking complex underlies the regular arrangement of outer arm dynein in the axoneme. Proceedings of the National Academy of Sciences of the United States of America 111, 9461–9466 (2014). [PubMed: 24979786]
28. Oda T, Abe T, Yanagisawa H, Kikkawa M, Docking-complex-independent alignment of *Chlamydomonas* outer dynein arms with 24-nm periodicity in vitro. Journal of cell science 129, 1547–1551 (2016). [PubMed: 26933181]
29. Heuser T, Raytchev M, Krell J, Porter ME, Nicastro D, The dynein regulatory complex is the nexin link and a major regulatory node in cilia and flagella. The Journal of cell biology 187, 921–933 (2009). [PubMed: 20008568]
30. Huang B, Ramanis Z, Luck DJ, Suppressor mutations in *Chlamydomonas* reveal a regulatory mechanism for Flagellar function. Cell 28, 115–124 (1982). [PubMed: 6461414]
31. Summers KE, Gibbons IR, Adenosine triphosphate-induced sliding of tubules in trypsin-treated flagella of *sea-urchin* sperm. Proceedings of the National Academy of Sciences of the United States of America 68, 3092–3096 (1971). [PubMed: 5289252]
32. Alford LM, Stoddard D, Li JH, Hunter EL, Tritschler D, Bower R, Nicastro D, Porter ME, Sale WS, The nexin link and B-tubule glutamylation maintain the alignment of outer doublets in the ciliary axoneme. Cytoskeleton 73, 331–340 (2016). [PubMed: 27105591]
33. Song K, Awata J, Tritschler D, Bower R, Witman GB, Porter ME, Nicastro D, In situ localization of N and C termini of subunits of the flagellar nexin-dynein regulatory complex (N-DRC) using SNAP tag and cryo-electron tomography. J Biol Chem 290, 5341–5353 (2015). [PubMed: 25564608]
34. von der Ecken J, Muller M, Lehman W, Manstein DJ, Penczek PA, Raunser S, Structure of the F-actin-tropomyosin complex. Nature 519, 114–117 (2015). [PubMed: 25470062]
35. Herrmann H, Aebi U, Intermediate Filaments: Structure and Assembly. Cold Spring Harbor perspectives in biology 8, (2016).
36. Lin J, Tritschler D, Song K, Barber CF, Cobb JS, Porter ME, Nicastro D, Building blocks of the nexin-dynein regulatory complex in *Chlamydomonas* flagella. The Journal of biological chemistry 286, 29175–29191 (2011). [PubMed: 21700706]
37. Bower R, Tritschler D, Mills KV, Heuser T, Nicastro D, Porter ME, DRC2/CCDC65 is a central hub for assembly of the nexin-dynein regulatory complex and other regulators of ciliary and flagellar motility. Molecular biology of the cell 29, 137–153 (2018). [PubMed: 29167384]

38. Wirschell M, Olbrich H, Werner C, Tritschler D, Bower R, Sale WS, Loges NT, Pennekamp P, Lindberg S, Stenram U, Carlen B, Horak E, Kohler G, Nurnberg P, Nurnberg G, Porter ME, Omran H, The nexin-dynein regulatory complex subunit DRC1 is essential for motile cilia function in algae and humans. Nature genetics 45, 262–268 (2013). [PubMed: 23354437]
39. Linck R, Fu X, Lin J, Ouch C, Schefter A, Steffen W, Warren P, Nicastro D, Insights into the structure and function of ciliary and flagellar doublet microtubules: tektins, Ca2+-binding proteins, and stable protofilaments. The Journal of biological chemistry 289, 17427–17444 (2014). [PubMed: 24794867]
40. Nicastro D, Fu X, Heuser T, Tso A, Porter ME, Linck RW, Cryo-electron tomography reveals conserved features of doublet microtubules in flagella. Proceedings of the National Academy of Sciences of the United States of America 108, E845–853 (2011). [PubMed: 21930914]
41. Dymek EE, Lin J, Fu G, Porter M, Nicastro D, Smith EF, PACRG and FAP20 form the inner junction of axonemal doublet microtubules and regulate ciliary motility. Molecular biology of the cell, mbcE19010063 (2019).
42. Sui H, Downing KH, Molecular architecture of axonemal microtubule doublets revealed by cryo-electron tomography. Nature 442, 475–478 (2006). [PubMed: 16738547]
43. Maheshwari A, Obbineni JM, Bui KH, Shibata K, Toyoshima YY, Ishikawa T, alpha- and beta-Tubulin Lattice of the Axonemal Microtubule Doublet and Binding Proteins Revealed by Single Particle Cryo-Electron Microscopy and Tomography. Structure 23, 1584–1595 (2015). [PubMed: 26211611]
44. Owa M, Uchihashi T, Yanagisawa HA, Yamano T, Iguchi H, Fukuzawa H, Wakabayashi KI, Ando T, Kikkawa M, Inner lumen proteins stabilize doublet microtubules in cilia and flagella. Nature communications 10, 1143 (2019).
45. Nogales E, Whittaker M, Milligan RA, Downing KH, High-resolution model of the microtubule. Cell 96, 79–88 (1999). [PubMed: 9989499]
46. Zheng SQ, Palovcak E, Armache JP, Verba KA, Cheng Y, Agard DA, MotionCor2: anisotropic correction of beam-induced motion for improved cryo-electron microscopy. Nature methods 14, 331–332 (2017). [PubMed: 28250466]
47. Turonova B, Schur FKM, Wan W, Briggs JAG, Efficient 3D-CTF correction for cryo-electron tomography using NovaCTF improves subtomogram averaging resolution to 3.4A. Journal of structural biology 199, 187–195 (2017). [PubMed: 28743638]
48. Geiger B, Spatz JP, Bershadsky AD, Environmental sensing through focal adhesions. Nature reviews. Molecular cell biology 10, 21–33 (2009). [PubMed: 19197329]
49. Harauz G, Van Heel M, Exact filters for general geometry three dimensional reconstruction. Optik 73, 146–156 (1986).
50. Rosenthal PB, Henderson R, Optimal determination of particle orientation, absolute hand, and contrast loss in single-particle electron cryomicroscopy. Journal of molecular biology 333, 721–745 (2003). [PubMed: 14568533]
51. Witman GB, Carlson K, Berliner J, Rosenbaum JL, *Chlamydomonas* flagella. I. Isolation and electrophoretic analysis of microtubules, matrix, membranes, and mastigonemes. The Journal of cell biology 54, 507–539 (1972). [PubMed: 4558009]
52. Iancu CV, Tivol WF, Schooler JB, Dias DP, Henderson GP, Murphy GE, Wright ER, Li Z, Yu Z, Briegel A, Gan L, He Y, Jensen GJ, Electron cryotomography sample preparation using the Vitrobot. Nature protocols 1, 2813–2819 (2006). [PubMed: 17406539]
53. Mastronarde DN, Automated electron microscope tomography using robust prediction of specimen movements. Journal of structural biology 152, 36–51 (2005). [PubMed: 16182563]
54. Kremer JR, Mastronarde DN, McIntosh JR, Computer visualization of three-dimensional image data using IMOD. Journal of structural biology 116, 71–76 (1996). [PubMed: 8742726]
55. Grigorieff N, FREALIGN: high-resolution refinement of single particle structures. Journal of structural biology 157, 117–125 (2007). [PubMed: 16828314]
56. Mindell JA, Grigorieff N, Accurate determination of local defocus and specimen tilt in electron microscopy. Journal of structural biology 142, 334–347 (2003). [PubMed: 12781660]

57. Fernandez JJ, Luque D, Caston JR, Carrascosa JL, Sharpening high resolution information in single particle electron cryomicroscopy. Journal of structural biology 164, 170–175 (2008). [PubMed: 18614378]
58. Biasini M, Bienert S, Waterhouse A, Arnold K, Studer G, Schmidt T, Kiefer F, Gallo Cassarino T, Bertoni M, Bordoli L, Schwede T, SWISS-MODEL: modelling protein tertiary and quaternary structure using evolutionary information. Nucleic acids research 42, W252–258 (2014). [PubMed: 24782522]
59. Pettersen EF, Goddard TD, Huang CC, Couch GS, Greenblatt DM, Meng EC, Ferrin TE, UCSF Chimera--a visualization system for exploratory research and analysis. Journal of computational chemistry 25, 1605–1612 (2004). [PubMed: 15264254]
60. Sigworth FJ, Principles of cryo-EM single-particle image processing. Microscopy 65, 57–67 (2016). [PubMed: 26705325]
61. Rickgauer JP, Grigorieff N, Denk W, Single-protein detection in crowded molecular environments in cryo-EM images. eLife 6, (2017).
62. Jensen KH, Brandt SS, Shigematsu H, Sigworth FJ, Statistical modeling and removal of lipid membrane projections for cryo-EM structure determination of reconstituted membrane proteins. Journal of structural biology 194, 49–60 (2016). [PubMed: 26835990]
63. Narita A, Mizuno N, Kikkawa M, Maeda Y, Molecular determination by electron microscopy of the dynein-microtubule complex structure. Journal of molecular biology 372, 1320–1336 (2007). [PubMed: 17761194]
64. Nakane T, Kimanius D, Lindahl E, Scheres SH, Characterisation of molecular motions in cryo-EM single-particle data by multi-body refinement in RELION. eLife 7, (2018).
65. Bykov YS, Schaffer M, Dodonova SO, Albert S, Plitzko JM, Baumeister W, Engel BD, Briggs JA, The structure of the COPI coat determined within the cell. eLife 6, (2017).
66. Zanetti G, Prinz S, Daum S, Meister A, Schekman R, Bacia K, Briggs JA, The structure of the COPII transport-vesicle coat assembled on membranes. eLife 2, e00951 (2013). [PubMed: 24062940]
67. Bartesaghi A, Merk A, Borgnia MJ, Milne JL, Subramaniam S, Prefusion structure of trimeric HIV-1 envelope glycoprotein determined by cryo-electron microscopy. Nature structural & molecular biology 20, 1352–1357 (2013).
68. Bock D, Medeiros JM, Tsao HF, Penz T, Weiss GL, Aistleitner K, Horn M, Pilhofer M, In situ architecture, function, and evolution of a contractile injection system. Science 357, 713–717 (2017). [PubMed: 28818949]
69. Cai S, Bock D, Pilhofer M, Gan L, The in situ structures of mono-, di-, and trinucleosomes in human heterochromatin. Molecular biology of the cell 29, 2450–2457 (2018). [PubMed: 30091658]

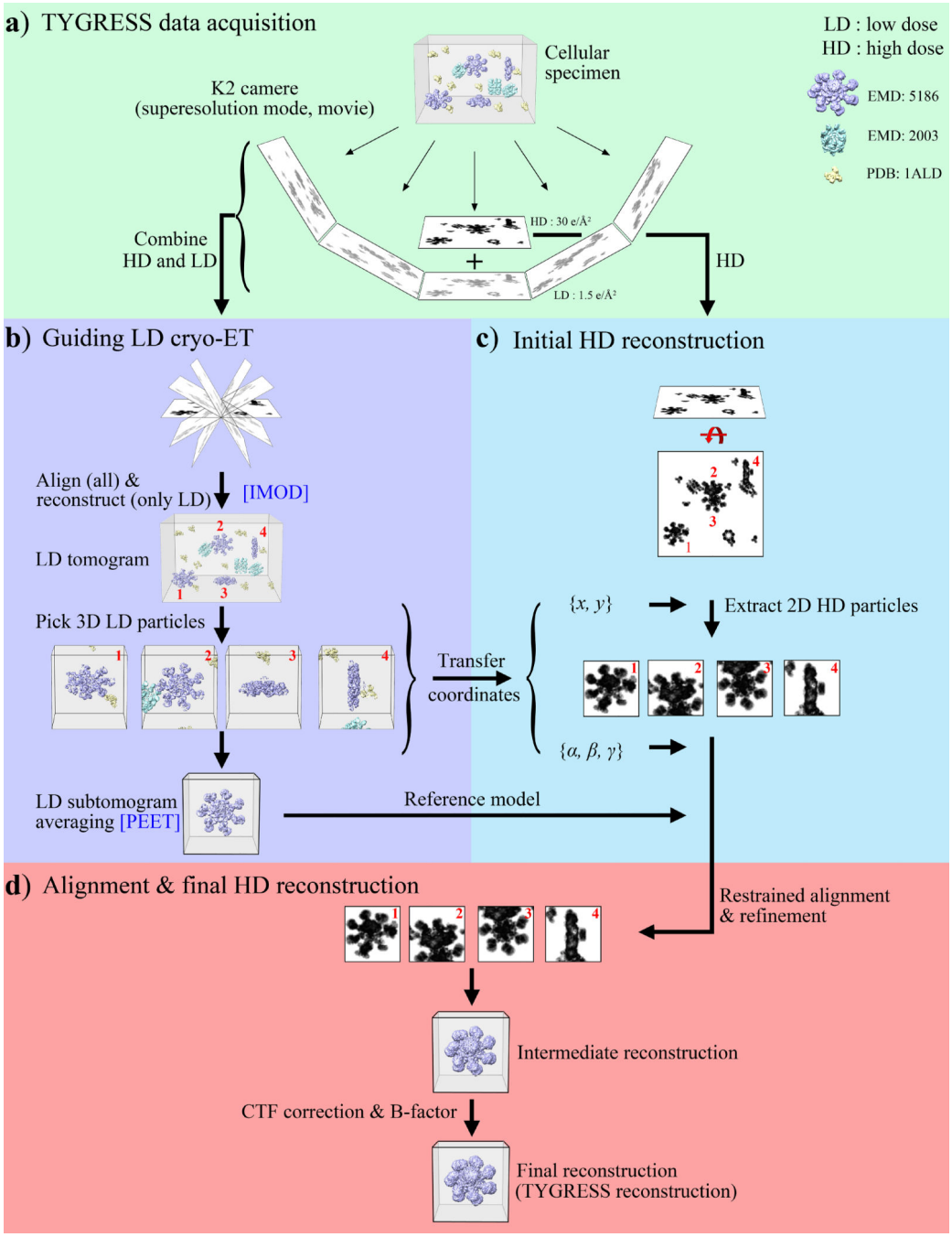

Figure 1. Overview of the TYGRESS workflow.

To simulate a 'cellular specimen', cryo-EM structures of the apoptosome (EMD: 5186, purple), GroEL (EMD: 2003, cyan), and aldolase (EMD: 1ALD, yellow), were randomly placed in a 3D volume. (**a**) A conventional single-particle image (HD image, ~30 e/Å^2) is recorded, followed by a tomographic tilt series (~1.5 e/Å^2 per LD image) of the same sample. (**b**) Both the LD images and the HD image are aligned. After alignment, only the LD images are used to reconstruct a tomogram, and particles of interest are picked and subjected to subtomogram averaging. (**c**) Particles of interest are picked in the HD image

using the coordinates $\{x, y\}$ and orientation $\{\alpha, \beta, \gamma\}$ derived from the tomogram in (**b**). (**d**) The particles picked from the HD image are aligned using their corresponding orientations and locations of the subtomograms. A CTF-corrected single-particle reconstruction is calculated from the particles in the HD image and used to further refine particle orientations and locations. Finally, a negative B-factor is applied to visualize high-resolution details.

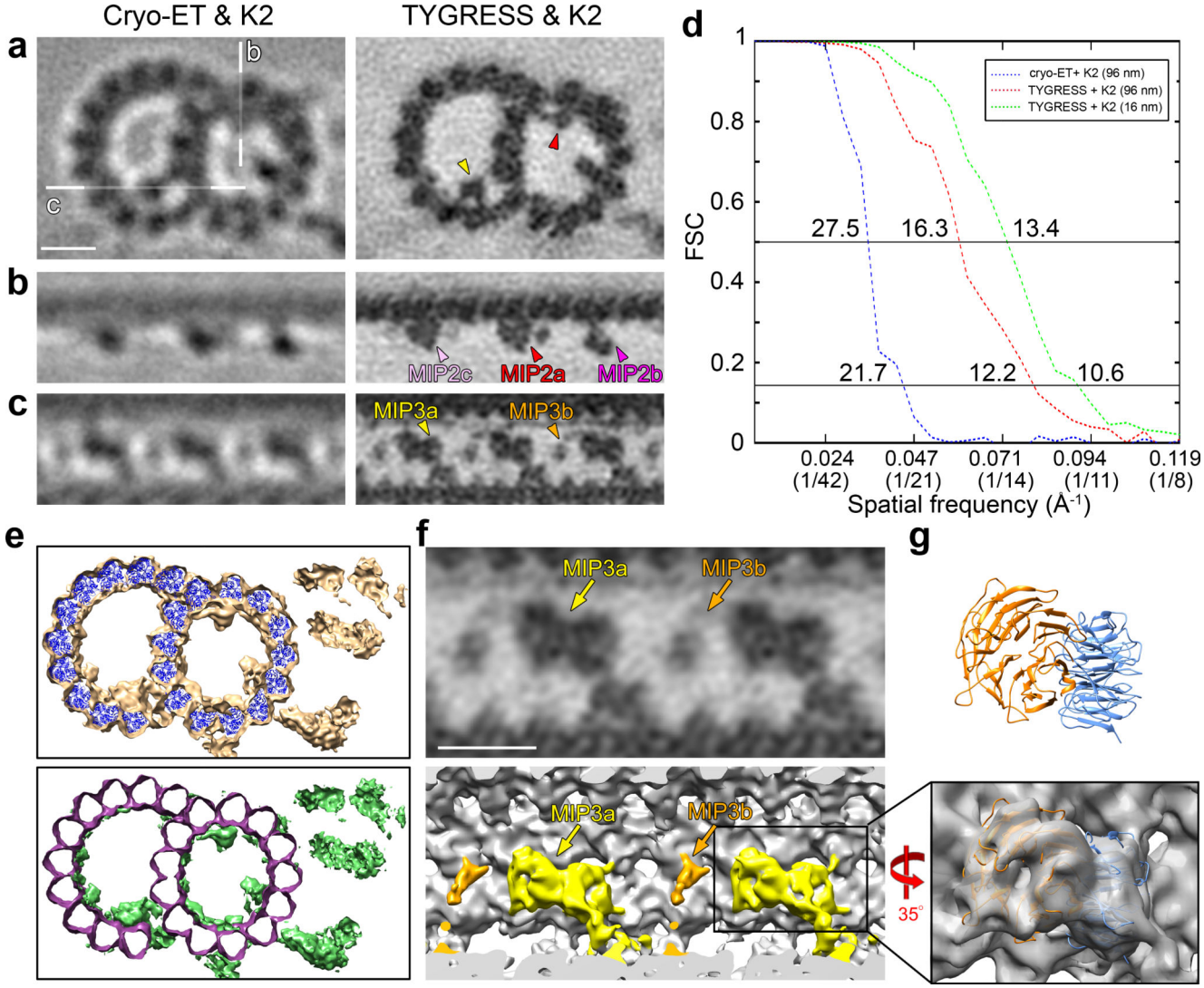

Figure 2. Comparison of doublet microtubules and MIPs visualized using different methods.

(**a-c**) Comparisons of EM slices of the *Tetrahymena* axonemal DMT obtained using cryo-ET (left column) and TYGRESS (right column), both using data collected on a K2 camera; cross-sectional (**a**; viewed from proximal) and longitudinal (**b** and **c**; proximal left) EM slices; white lines in (**a**, left) indicate the locations of the longitudinal slices (**b** and **c**). Scale bar: 10 nm. (**d**) Resolution estimates using the Fourier Shell Correlation (FSC)[49] of 2 independent halves of the dataset are shown for the cryo-ET/subtomogram average of the 96-nm repeat (blue; particle # 19,830), and two TYGRESS averages, i.e. for the 96-nm repeat (red; # 18,857) and the 16-nm microtubule repeat (green; # 112,386); sub-averaging the 16 nm repeat further improves the final resolution from 12.2 Å to 10.6 Å at the 0.143 FSC criterion[50]. (**e**) A difference map (bottom, green) was calculated between the *Tetrahymena* DMT structure obtained with TYGRESS (top, beige) and a docked pseudo-atomic model with tubulin dimers (top, blue). The remaining density (bottom, green) represents MAPs and MIPs attached to the microtubule walls. (**f**) EM slice (top) and 3D isosurface rendering (bottom) of MIP3a (yellow) and MIP3b (orange) after averaging the 16-

nm repeats. Scale bar: 10 nm. (**g**) A predicted pseudo-atomic model of FAP52 (top) with two beta-propellers was docked to our MIP3a density using the Chimera software package (bottom).

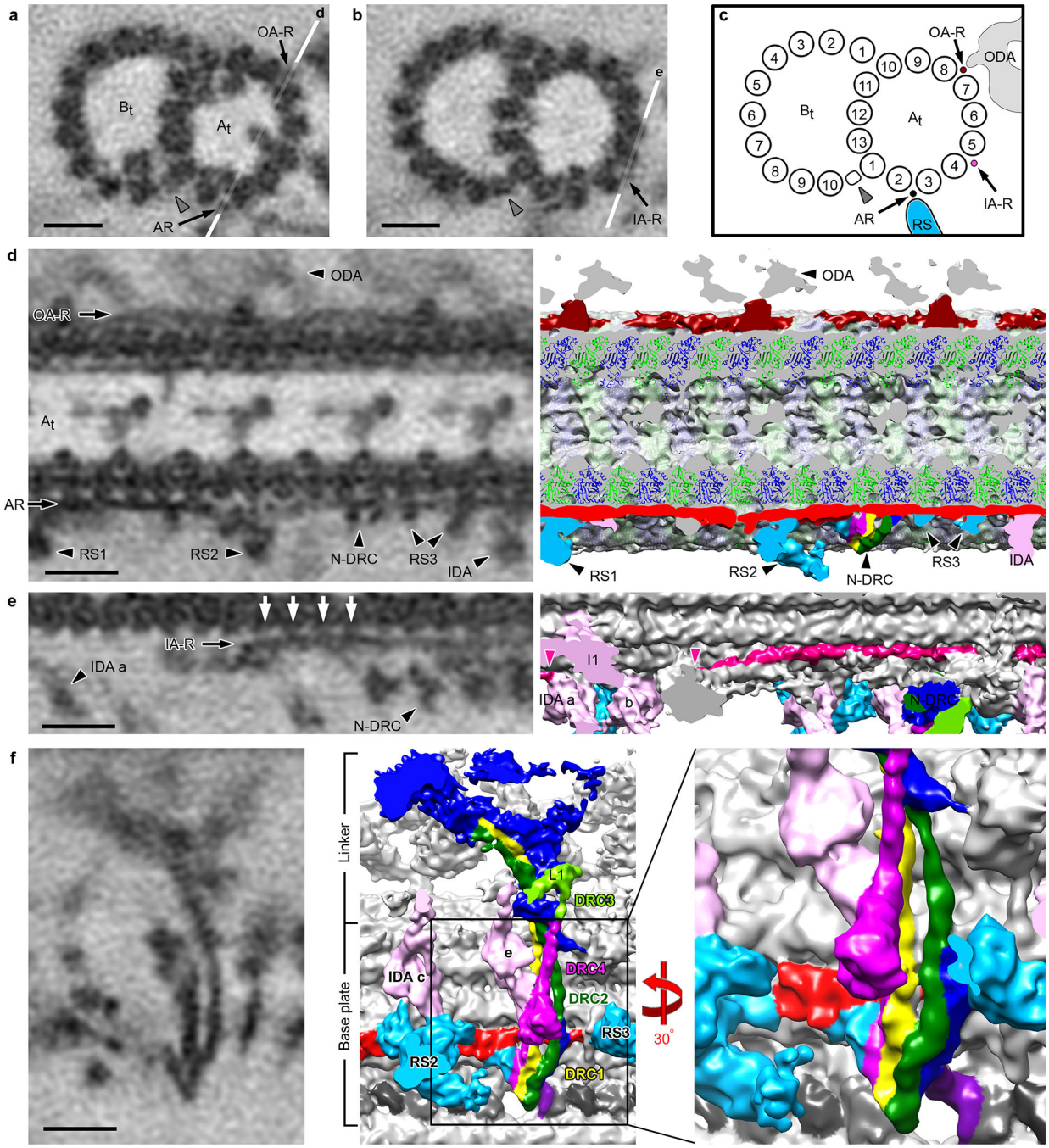

Figure 3. Filamentous structures and subunit architecture of the nexin-dynein regulatory complex (N-DRC) visualized by TYGRESS.

(**a** and **b**) Cross-sectional EM slices of averaged 96-nm axonemal repeats in two different positions showing three well-resolved filamentous structures: the 24-nm outer dynein arm ruler-like structure (OA-R), the 96-nm axonemal ruler (AR), and the inner dynein arm ruler-like structure (IA-R). White lines indicate the locations of the EM slices shown in (**d** and **e**); gray arrowhead: inner junction (IJ). (**c**) Schematic diagram showing the locations of the OA-R, AR, IA-R, and IJ (gray arrowhead). Other labels: ODA, outer dynein arm; A_t/B_t, A- and

B-tubule; RS, radial spoke. (**d**) Longitudinal EM slice (left) and 3D isosurface rendering (right) of the 96-nm axonemal repeat showing the OA-R (dark red) and AR (red). A tubulin dimer model is fitted into the microtubule density (positions of α/β-tubulin on the DMT according to ref. [43]). The three RSs 1–3 (light blue), N-DRC components (purple, yellow, and dark green), and inner dynein arms (IDAs, rose) are assembled onto the DMT through the AR. (**e**) Longitudinal EM slice (left) and 3D isosurface rendering (right) of the 96-nm axonemal repeat showing the IA-R (magenta). The IA-R starts between the RS1 and RS2 (right magenta arrowhead) and attaches to and stretches along the microtubule, connecting to the tail of the inner dynein arm a (left magenta arrowhead). (**f**) EM slice (left) and 3D isosurface rendering (middle, and zoom-in: right) of the N-DRC structure. The coiled-coil strands of the filamentous DRC 1, 2, and 4 are well resolved, comprising the base plate of the N-DRC, which contacts the 96-nm ruler (red) and the DMT and expands to the linker domain of the N-DRC; DRC1, yellow; DRC2, dark green; DRC3, light green; DRC4, purple. Unknown N-DRC components are shown in dark blue. Other labels: tails of inner dynein arm IDA c and e, pink; bases of RS2 and RS3, light blue. Scale bars: 10 nm.

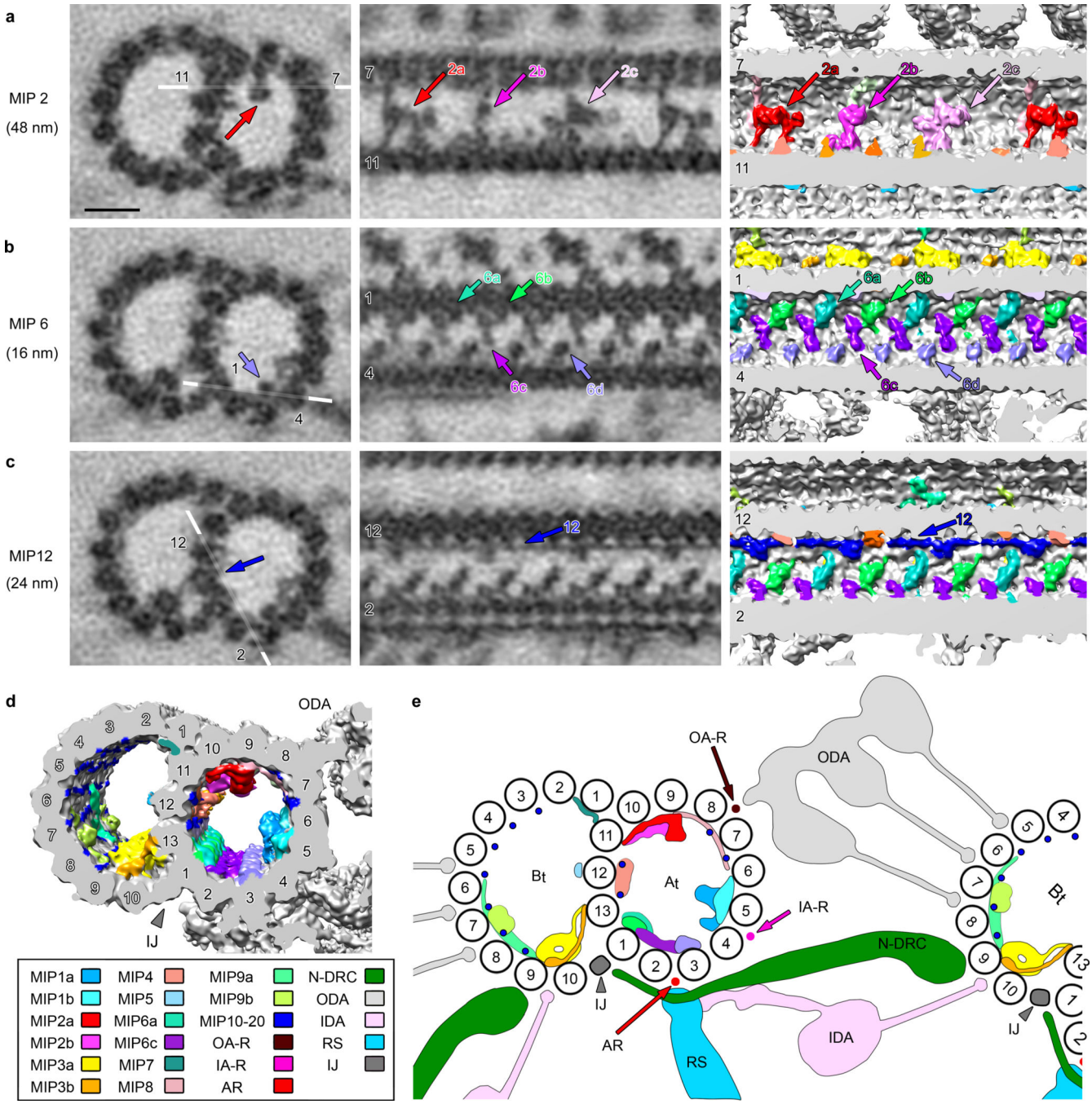

Figure 4. MIP structures in the intact *Tetrahymena* axonemes resolved by TYGRESS.

(**a-c**) Cross-sectional (left column) and longitudinal (middle column) EM slices and longitudinal 3D isosurface renderings (right column) of the averaged DMT show the structural details and diversity of selected MIP complexes (color coded as shown in **d**). White lines in the cross-sections indicate the locations of the respective longitudinal EM slices. Selected protofilament numbers are indicated. MIP periodicities are indicated by the numbers inside the brackets on the left. Scale bar: 10 nm. (**d**) The 3D isosurface rendering of the 96-nm axonemal repeat shows the locations of 20 MIP structures in the cross-sectional

view. MIPs are colored and numbered according to their locations; gray arrowhead: inner junction (IJ). (**e**) Schematic summary showing the locations and interactions of axonemal complexes and protofilaments (numbered). Other labels: A_t/B_t, A- and B-tubule; IJ, inner junction; AR, axonemal ruler; OA-R, outer dynein arm ruler-like structure; IA-R, inner dynein arm ruler-like structure; RS, radial spoke; IDA/ODA, inner dynein arm/outer dynein arm; N-DRC, nexin-dynein regulatory complex; MIPs, microtubule inner proteins.